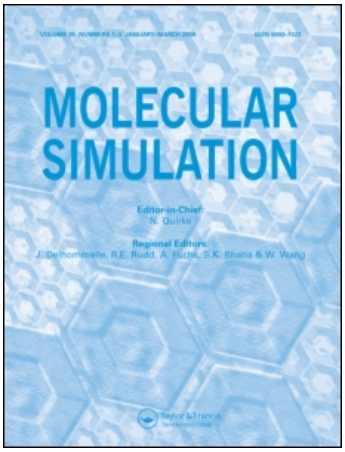

Molecular Simulation
Publication details, including instructions for authors and subscription information:
http://www.informaworld.com/smpp/title~content=t713644482

Effect of partial charge parameterization on the phase equilibria of dimethyl ether

M. B. H. Ketko[a]; J. J. Potoff[a]
[a] Department of Chemical Engineering and Materials Science, Wayne State University, Detroit, MI, USA

To cite this Article Ketko, M. B. H. and Potoff, J. J.(2007) 'Effect of partial charge parameterization on the phase equilibria of dimethyl ether', Molecular Simulation, 33: 9, 769 — 776
To link to this Article: DOI: 10.1080/08927020701275076
URL: http://dx.doi.org/10.1080/08927020701275076

Molecular Simulation, Vol. 33, Nos. 9–10, 15–30 August 2007, 769–776

Taylor & Francis
Taylor & Francis Group

Effect of partial charge parameterization on the phase equilibria of dimethyl ether

M. B. H. KETKO and J. J. POTOFF*

Department of Chemical Engineering and Materials Science, Wayne State University, Detroit, MI 48202, USA

(Received December 2006; in final form February 2007)

The effect of partial charge parameterization on the fluid phase behavior of dimethyl ether (DME) is investigated with grand canonical Monte Carlo simulations coupled with histogram reweighting techniques. A total of 16 optimized parameter sets are presented, covering a range of dipole moments from 0 to 2.4 D. Although all 16 parameter sets are able to reproduce experimental saturated liquid densities, only six of the parameter sets, corresponding to $-0.433 \leq q_O \leq -0.58$ are able to simultaneously produce accurate predictions for the saturated liquid densities and vapor pressures over the temperature range $280 \leq T \leq 380$. The heat of vaporization, acentric factor and radial distributions are also presented.

Keywords: Force field; Dimethyl ether; Simulation; Phase behavior

1. Introduction

Over the last two decades, a tremendous effort has taken place in the development of high accuracy molecular models or "force fields" for use in computer simulations. The method of parameterization varies depending on the target data of interest. For example, parameters for the MMFF force field [1] were determined by fitting to reproduce crystal structure data, while non-bonded interactions in the optimized potentials for liquid simulations (OPLS) [2] were optimized to reproduce the properties such as liquid density and heat of vaporization for organic molecules near ambient conditions. However, even among force fields developed to study a particular class of problems, e.g. biomolecular systems [2–5] or phase behavior [6–9], significant differences can be found amongst the reported parameter sets.

Previous calculations performed by our group for CO_2 [10], H_2S [11] and acetone [12] have identified multiple combinations of partial charge distributions and Lennard–Jones parameters that yield an accurate reproduction of the pure component vapor–liquid coexistence curves and vapor pressures for these molecules. In each of the previously mentioned cases, the optimization procedure was restricted to the region around "correct" values of the partial charges, which were generally determined by fitting to reproduce gas phase dipole or quadrupole moments or taken from a CHELPG analysis of *ab initio* calculations.

The purpose of this paper is to demonstrate conclusively the non-uniqueness of force field parameter sets, and to illustrate how specific physical property data may be used effectively in the optimization of force field parameters for real fluids. In this case, dimethyl ether (DME) was selected as the target molecule for the force field development. In addition to the geometric simplicity of the molecule, DME has a number of important technological applications including low temperature refrigeration [13], cryogenic storage [13] and oxygenated fuels [14,15].

In this work, 16 optimized parameter sets are presented for DME, covering a range of dipole moments μ from 0 to 2.4 D. For a given distribution of partial charges, parameters representing the dispersive interactions are optimized such that the predictions of simulation are in close agreement with experimentally determined saturated liquid densities. Saturated liquid and vapor densities, vapor pressures and heat of vaporization are determined with histogram-reweighting Monte Carlo simulations in the grand canonical ensemble [16] and compared to experimental values. Additional calculations in the isobaric–isothermal ensemble are used to determine radial distribution functions (RDF).

*Corresponding author. Email: jpotoff@chem1.eng.wayne.edu

Molecular Simulation
ISSN 0892-7022 print/ISSN 1029-0435 online © 2007 Taylor & Francis
http://www.tandf.co.uk/journals
DOI: 10.1080/08927020701275076

This work is organized as follows. In the next section, the form of the energy function describing the interactions between atoms in DME is described. In Section 3, the relevant simulation details are presented. Vapor–liquid coexistence curves, vapor pressures, heat of vaporization and RDF are presented in Section 4. The conclusions of this work can be found in Section 5.

2. Models and simulation details

2.1 Force fields

In this work, DME is modeled with three interaction sites centered at the nuclei of the oxygen and carbon atoms. Hydrogens bonded to carbon atoms are not modeled explicitly. Instead, the united-atom approximation is used where hydrogen and carbon atoms are lumped together to form a single interaction site known as a "pseudo-atom". Interactions between pseudo-atoms in different molecules are represented by pairwise-additive Lennard–Jones 12–6 potentials and Coulombic interactions of partial charges

$$U(r_{ij}) = 4\varepsilon_{ij}\left[\left(\frac{\sigma_{ij}}{r_{ij}}\right)^{12} - \left(\frac{\sigma_{ij}}{r_{ij}}\right)^{6}\right] + \frac{q_i q_j}{4\pi\varepsilon_0 r_{ij}} \quad (1)$$

where r_{ij}, ε_{ij}, σ_{ij}, q_i and q_j are the separation, LJ well depth, LJ size and partial charges, respectively, for the pair of interaction sites i and j. ϵ_0, which has a value of 8.854×10^{-12} F/m, is the permittivity of vacuum. The Lennard–Jones parameters and partial charges for each of the 16 parameter sets developed in this work are listed in table 1. Interactions between atoms of different types are determined with the standard Lorentz–Berthelot combining rules [17,18].

$$\sigma_{ij} = \frac{\sigma_{ii} + \sigma_{jj}}{2} \quad (2)$$

$$\varepsilon_{ij} = \sqrt{\varepsilon_{ii}\varepsilon_{jj}} \quad (3)$$

Oxygen and CH_3 pseudo-atoms are connected with a fixed bond length of 1.41 Å. Bond bending for the CH_3—O—CH_3 bond angle is controlled with a harmonic potential

$$U_{\text{bend}} = \frac{k_\theta}{2}(\theta - \theta_0)^2 \quad (4)$$

where $k_\theta/k_B = 60{,}400$ K/rad^2 is the bending constant, θ and $\theta_0 = 112°$ are the instantaneous and equilibrium bond angle, respectively. Parameters for all bonded interactions were taken from the TraPPE force field [19].

Table 1. Parameters for non-bonded interactions used in this work.

Force field	*Pseudo-atom*	*ε (K)*	*σ (Å)*	*q (e)*
All models	CH_3	98.0	3.75	$q_c = 0.5\lvert q_O\rvert$
Model 1	O	110.0	2.8	0.0
Model 2	O	95.0	2.95	−0.1
Model 3	O	95.0	2.93	−0.2
Model 4	O	77.0	3.15	−0.3
Model 5	O	74.0	3.1	−0.35
Model 6	O	72.0	3.0	−0.4
Model 7	O	57.0	3.3	−0.433
Model 8	O	57.0	3.15	−0.445
Model 9	O	58.0	3.1	−0.45
Model 10	O	55.0	3.1	−0.47
Model 11	O	47.0	3.1	−0.51
Model 12	O	47.0	3.0	−0.52
Model 13	O	43.0	3.1	−0.53
Model 14	O	40.0	3.1	−0.54
Model 15	O	35.0	2.8	−0.58
Model 16	O	23.0	3.2	−0.62

3. Simulation details

Grand canonical histogram-reweighting Monte Carlo (GCMC) simulations [16] were used to determine the vapor–liquid coexistence curves and vapor pressures for DME. The insertion of molecules in the GCMC simulations was enhanced through the application of the coupled–decoupled configurational-bias Monte Carlo method [20]. The fractions of the various moves for each simulation were set to 15% for particle displacements, 15% for rotations, 10% configurational-bias regrowths and 60% for insertions and deletions. All simulations was performed for a system size of $L = 20$ Å. Lennard–Jones interactions were truncated at $L = 10$ Å, and standard long-range corrections were applied [21,22]. An Ewald sum with tinfoil boundary conditions ($\kappa \times L = 5$ and $K_{\max} = 5$) was used to calculate the long range electrostatic interactions [23,24]. Simulations were equilibrated for 1 million Monte Carlo steps (MCS) before run statistics were recorded. After the equilibration period, histograms were collected from simulations that were 25×10^6 MCS in length. Over the course of each simulation, the number of molecules N and energy E were stored in the form of a list [25], which was updated every 250 MCS. The necessary probability distributions were extracted from this list after the completion of the simulation.

4. Results and discussion

The purpose of this work is to demonstrate the non-uniqueness of force field parameters, and to map parameter space in terms of Lennard–Jones parameters and partial charges that yield an accurate representation of the saturated liquid densities, critical point, vapor pressures and heat of vaporization for DME. Models were developed as follows. Lennard–Jones parameters for the CH_3 pseudo-atom were taken directly from the TraPPE force field and held fixed. For a given oxygen partial charge, corresponding charges were placed on the methyl groups to maintain charge neutrality. The Lennard–Jones parameters for the oxygen atom were then optimized such that the deviation of simulation from the experimental saturated liquid densities was minimized. Overall, a total of 16 optimized parameter sets are presented, which corresponds to a range of dipole moments from 0 to 2.4 D

($0 \leq q_O \leq -0.62$). Above $\mu = 2.4$ D it was no longer possible to achieve an accurate representation of the saturated liquid densities.

4.1 Vapor–liquid equilibria

In figure 1, the vapor–liquid coexistence curves predicted by the 16 force fields are presented. The data show that the distribution of partial charges has little effect on the predicted saturated liquid densities over the temperature range 280–380 K, as long as the oxygen ε_O and σ_O are reparameterized accordingly. As shown in table 1, as the partial charge was increased, ε_O was reduced monotonically. This was expected, since increasing the partial charge also increases the interaction between molecules. To reproduce the experimental critical temperature, ε_O had to be reduced such that the overall molecule–molecule interactions remained the same. This resulted in a shift of interactions from being primarily dispersive to having a significant Coulombic component as the dipole moment was increased. Unlike the case for the Lennard–Jones well-depth, the collision diameter σ_O remained nearly constant, varying between 2.8 and 3.2 Å, although small adjustments were necessary to reproduce the saturated liquid densities.

Based on these results, it is clear that optimizing potential parameters to reproduce only the saturated liquid densities, even over a wide range of temperatures, does not provide enough information to uniquely determine the "correct" distribution of partial charges. Previous calculations for two-center Lennard–Jones fluids with embedded point quadrupoles [26] or dipoles [27] have shown that quadrupole and dipole moments have a significant effect on the acentric factor, which is defined as

$$\omega = -\log_{10} P_r^{\text{sat}} - 1 \tag{5}$$

where P_r^{sat} is evaluated at $T_r = 0.7$. It has been shown experimentally that the acentric factor is a function of both molecule shape/size and dipole moment [28,29]. Therefore, it is instructive to examine the effect of partial charge distribution on the predicted vapor pressures for DME.

The vapor pressures predicted by each of the 16 force fields are presented in the form of Clausius–Clapeyron plots in figure 2. As expected, the distribution of partial charges has a significant impact on the predicted vapor pressures and acentric factors. For the six parameter sets with $-0.433 \leq q_O \leq -0.58$, the predicted vapor pressures are within 1% of experimental data. For parameter sets with $q_O > -0.433$, vapor pressures are over-predicted, while parameter sets with $q_O < -0.58$ resulted in an under-prediction of the vapor pressure. The largest deviation from experiment was 28%, which occurred for Model 1.

To further illustrate the impact of dipole moment on acentric factor, the acentric factors predicted by each force field are plotted versus dipole moment in figure 3. The data show that as the dipole moment is increased, the acentric factor also increases. Although some scatter exists in the data, due in part to the process of fitting to the

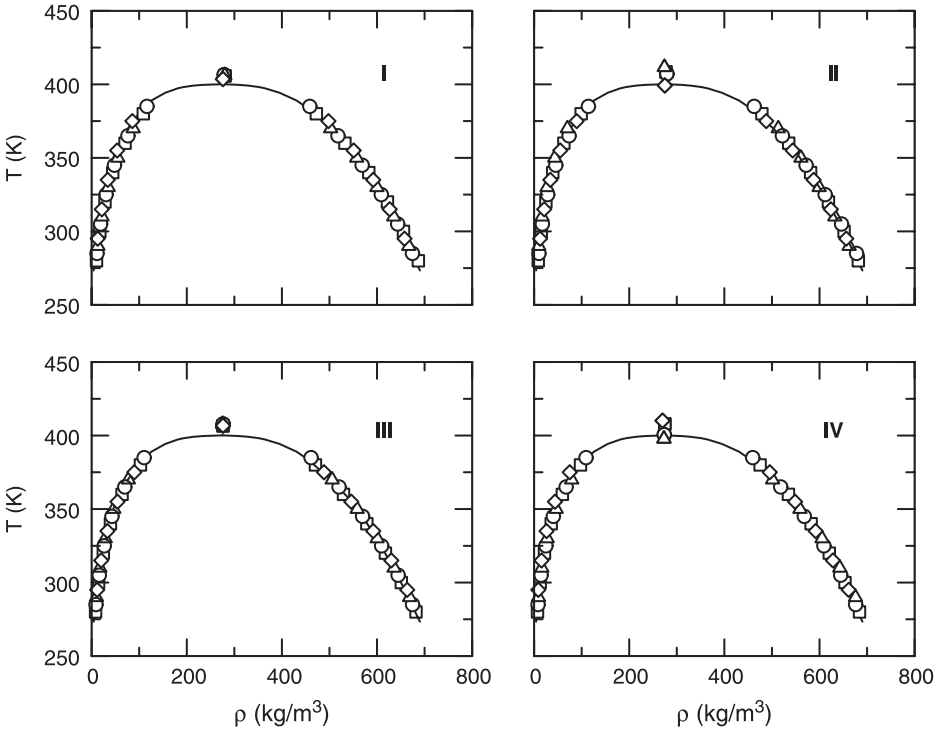

Figure 1. Vapor–liquid coexistence curves predicted by simulation for DME. Experiment [44] is represented by a "solid line". Plot (I) contains model 1 (squares), model 2 (circle), model 3 (triangles) and model 4 (diamonds). Plot (II) contains model 5 (squares), model 6 (circle), model 7 (triangles) and model 8 (diamonds). Plot (III) contains model 9 (squares), model 10 (circle), model 11 (triangles) and model 12 (diamonds). Plot (IV) contains model 13 (squares), model 14 (circle), model 15 (triangles) and model 16 (diamonds).

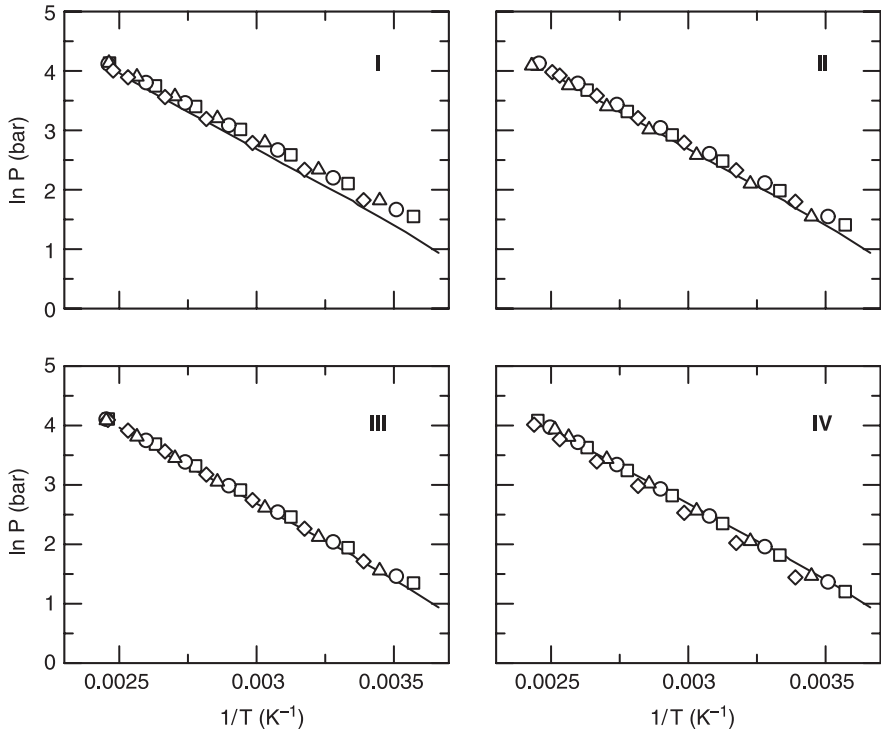

Figure 2. Clausius–Clapeyron plot for DME. Experiment [44] is represented by a "solid line". Plot (I) contains model 1 (squares), model 2 (circle), model 3 (triangles) and model 4 (diamonds). Plot (II) contains model 5 (squares), model 6 (circle), model 7 (triangles) and model 8 (diamonds). Plot (III) contains model 9 (squares), model 10 (circle), model 11 (triangles) and model 12 (diamonds). Plot (IV) contains model 13 (squares), model 14 (circle), model 15 (triangles) and model 16 (diamonds).

saturated liquid densities, the acentric factor increases quadratically with respect to dipole moment. In order to reproduce the experimentally determined acentric factor $\omega = 0.19$ [30], the dipole moment had to be increased to 2.04 D ($q_O = -0.54$), which is 57% larger than the experimentally measured gas phase dipole moment of 1.3 D. The need to specify a dipole moment larger than the experimentally measured gas phase dipole moment stems from the fact that the Lennard–Jones plus point charge functional form used in this work is an effective potential function, where the parameters account for multiple types of interactions, such as dipole–dipole and dipole–quadrupole. Furthermore, these parameters represent the interactions between molecules/functional groups averaged over liquid phase and vapor phases for a wide range of thermodynamic state points.

4.2 Critical properties

Critical parameters for each of the force fields, listed in table 2, were determined by fitting the saturated liquid and vapor densities over the temperature range $280 \leq T \leq 380$ K to the density scaling law for critical temperature [31]

$$\rho_{liq} - \rho_{vap} = B(T - T_c)^{\beta} \tag{6}$$

and the law of rectilinear diameters [32]

$$\frac{\rho_{liq} + \rho_{vap}}{2} = \rho_c + A(T - T_c) \tag{7}$$

where $\beta = 0.325$ is the critical exponent for Ising-type fluids in three dimensions [33] and A and B are constants fit to simulation data. All of the force fields were found to yield an accurate reproduction of the experimental critical temperature and density. The maximum relative error of 3% in T_c was produced by Model 7 ($q_O = -0.433$), while the maximum error of 2% in ρ_c was given by Model 1 ($q_O = 0$). No clear trends in the prediction of the critical temperature with respect to partial charge distribution were found. On the other hand, the error in ρ_c was reduced as the dipole moment was increased.

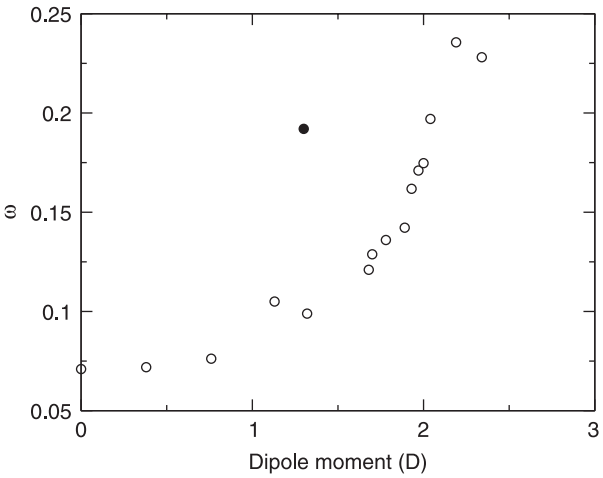

Figure 3. Acentric factor versus dipole moment for all 16 models of DME where the experimental acentric factor versus dipole moment is symbolized by a "solid circle" [30].

Table 2. Predicted normal boiling points, critical properties and acentric factor for DME.

	T_b (K)	T_c (K)	ρ_c (kg/m^3)	P_c (bar)	ω
Experiment [44]	249	400.2	275	52.8	0.19
Model 1	236.47	405.76	280.34	62.32	0.07
Model 2	237.33	406.58	278.76	61.56	0.07
Model 3	237.15	406.16	279.77	62.43	0.08
Model 4	241.25	403.59	276.02	55.05	0.11
Model 5	240.99	408.39	277.44	61.21	0.10
Model 6	241.81	407.12	279.13	62.19	0.12
Model 7	246.21	411.66	274.01	59.67	0.13
Model 8	243.17	399.27	274.81	53.55	0.16
Model 9	243.27	406.57	276.26	60.94	0.14
Model 10	244.61	407.81	276.31	60.80	0.14
Model 11	246.67	407.70	275.51	59.61	0.16
Model 12	246.69	406.74	276.14	59.96	0.17
Model 13	247.91	407.84	274.95	59.42	0.17
Model 14	247.90 ± 0.3	400.57 ± 0.2	273.71 ± 0.2	53.17 ± 0.1	0.20 ± 0.001
Model 15	250.11	397.77	272.91	51.03	0.24
Model 16	255.33	410.14	270.19	55.36	0.23

Representative statistical uncertainties are shown for Model 14.

Linear extrapolation of the vapor pressure curve to the critical temperature, as predicted by simulation, was used to determine the critical pressure for each parameter set. Relative deviations of simulation from experiment were more pronounced in the case of the critical pressure, with the maximum error in P_c equal to 18%, given by Model 1. Only five parameter sets (Models 4, 8 and 14–16) were able to produce a critical pressure within 5% of experiment. The best prediction of the critical pressure was given by Model 14($q_O = -0.54$), which yields $P_c = 53.17$ bar compared to the experimental value of 52.8 bar. Due to the extrapolation to the T_c predicted by simulation and the rapid increase of the pressure with respect to temperature in the critical region, the error in P_c is amplified by errors in T_c.

The normal boiling points, listed in table 2, were also derived from the Clausius Clapeyron plots, this time by extrapolation to 1.01 bar. The maximum error in T_b was 5%, given by Model 1, while many of the parameter sets were capable of predicting T_b within 1% of experiment. Although scatter is present, the general trend of the data shows that the error in the prediction of T_b decreases as the dipole moment increases.

4.3 Heat of vaporization

The heat of vaporization ΔH_v was calculated for each parameter set over the temperature range $240 < T < 380$. These results are shown in figure 4. Since the enthalpy is defined as

$$H = U + pV \tag{8}$$

ΔH_v can be calculated directly from

$$\Delta H_v = U_v - U_l + p(V_v - V_l) \tag{9}$$

where the v and l subscripts refer to the vapor and liquid phases, U is the internal energy per mol and V is the molar volume. The energies and molar volumes of each phase were determined from the same histogram data collected for the VLE calculations. The predictions of simulation for heat of vaporization were found to be in excellent agreement with the experimental values of 21.51 kJ/mol at 248.2 K [34], and 18.51 kJ/mole at 298.15 K [35] for each of the force fields that also yielded an accurate description of the vapor pressure as a function of temperature. Inspection of the Clapeyron equation

$$\frac{dP^{sat}}{dT} = \frac{\Delta H_v}{T(V_g - V_l)} \tag{10}$$

illustrates why. In cases where the saturated liquid and vapor densities and the vapor pressures are in close agreement with experiment over a wide range of temperatures, then the heat of vaporization must also agree with experimental results.

4.4 *Ab initio* calculations

Ab initio calculations are commonly used to determine partial charges for use in atomistic force fields. Due to the wide range of partial charge distributions presented in this work, an effective comparison can be made without reparameterization of the force fields.

The geometry of DME was optimized at the HF/6 − 31 + g(d,p) and MP2/6 − 31 + g(d,p) levels of theory and basis set. The partial charges for the CH_3 and O pseudo-atoms were determined through the application of the CHELPG methodology to the electrostatic potential energy surfaces determined by *ab initio* calculations [36–38]. These calculations were performed with the Gaussian 03 software [39]. The CHELPG scheme was selected for comparison as it has recently become the method of choice for the determination of partial charge distributions for a number of atomistic force fields [12,40–43]. Calculations were performed in vacuum at the HF/6 − 31 + g(d,p) and MP2/6 − 31 + g(d,p) levels of theory and basis set, which resulted in partial charges of $q_O = -0.445$ (HF) and $q_O = -0.433$ (MP2). These results fall on the edge of the region where the force

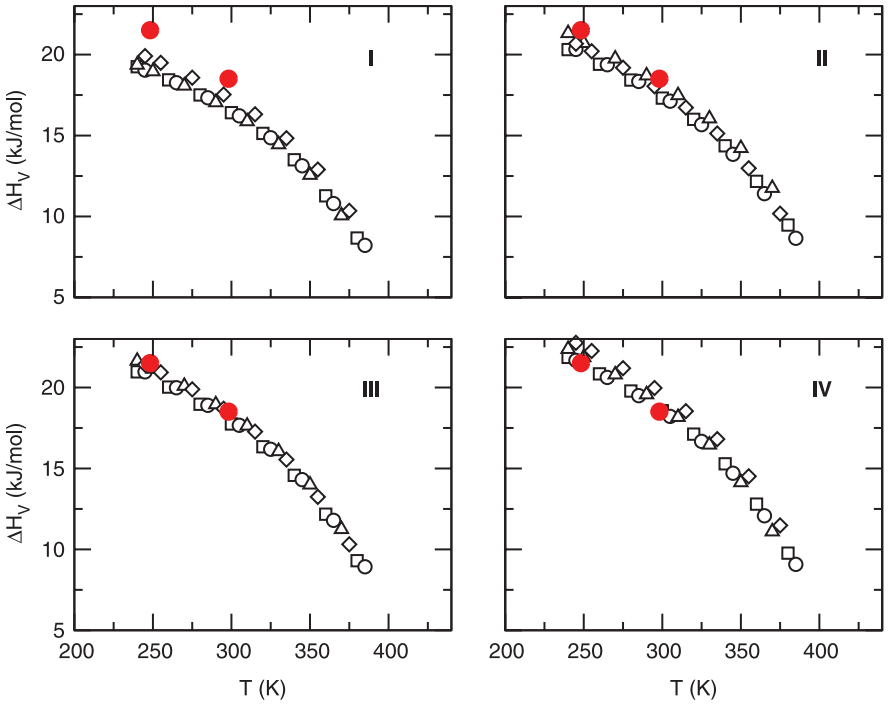

Figure 4. Heat of vaporization as a function of temperature for DME. The experimental data [35] is denoted as red circles. Plot (I) contains model 1 (squares), model 2 (circle), model 3 (triangles) and model 4 (diamonds). Plot (II) contains model 5 (squares), model 6 (circle), model 7 (triangles) and model 8 (diamonds). Plot (III) contains model 9 (squares), model 10 (circle), model 11 (triangles) and model 12 (diamonds). Plot (IV) contains model 13 (squares), model 14 (circle), model 15 (triangles) and model 16 (diamonds).

field is able to fit both the saturated liquid density and vapor pressure. Although these partial charges yield a good description of the phase behavior and vapor pressure for DME, the best reproduction of experimental data by the proposed force fields occurs for Model 14, where the magnitude of the partial charges are approximately 10% larger than those predicted by *ab initio* calculations at the HF/6 − 31 + g(d,p) level. These results are similar to differences between empirical "best fit" and *ab initio* derived partial charges determined in the parameterization of H_2S [11].

4.5 Radial distribution functions

In order to determine the effect of dipole moment on the liquid structure of DME, *NPT* simulations were performed at 300 K and 1 bar. The RDF were extracted from the configurations saved during the simulations. Figures 5 and 6 show the RDF for methyl–oxygen and oxygen–oxygen interactions for each of the parameter sets. The data show that optimizing ε_O and σ_O to reproduce the vapor–liquid coexistence curve and vapor pressure for each set of partial charges results in identical RDF.

5. Conclusions

A suite of 16 parameter sets have been optimized for DME, each corresponding to a specific dipole moment from 0 to 2.4 D. The data demonstrate clearly the non-uniqueness of potential parameters. All 16 parameter sets could be optimized to reproduce the saturated liquid density, while only six parameter sets were capable of reproducing the vapor pressure to within 1% of experiment in addition to the saturated liquid densities. Parameter sets that were able to reproduce saturated liquid densities and vapor pressures were also found to yield excellent predictions of the heat of vaporization as a function of temperature. All of the models were able to reproduce T_c and ρ_c to within 5% of experiment, and a handful of parameter sets were able to predict T_c and ρ_c for DME with less than 1% error. Regarding the acentric factor, comparison of simulation data to experiment revealed that a significant increase in the dipole moment was necessary to reproduce the experimental value of $\omega = 0.19$. RDF, determined from *NPT* simulations, showed that the changing the dipole moment had no effect on the liquid phase structure.

Based on these results, it is clear that saturated liquid densities should not be used alone in the parameterization of force fields. The inclusion of the vapor pressure in the parameterization is an effective means for reducing the number of candidate parameter sets, since the vapor pressure and acentric factors are strong functions of the dipole moment. On the other hand, the heat of vaporization ΔH_v, a target parameter used commonly in the development of force fields for biological systems, was not found to provide any additional insight beyond what could be gleaned from the saturated densities and vapor pressure. Despite the inclusion of vapor pressure in this work, there were still six viable parameter sets. In previous studies, the use of binary mixtures to provide additional

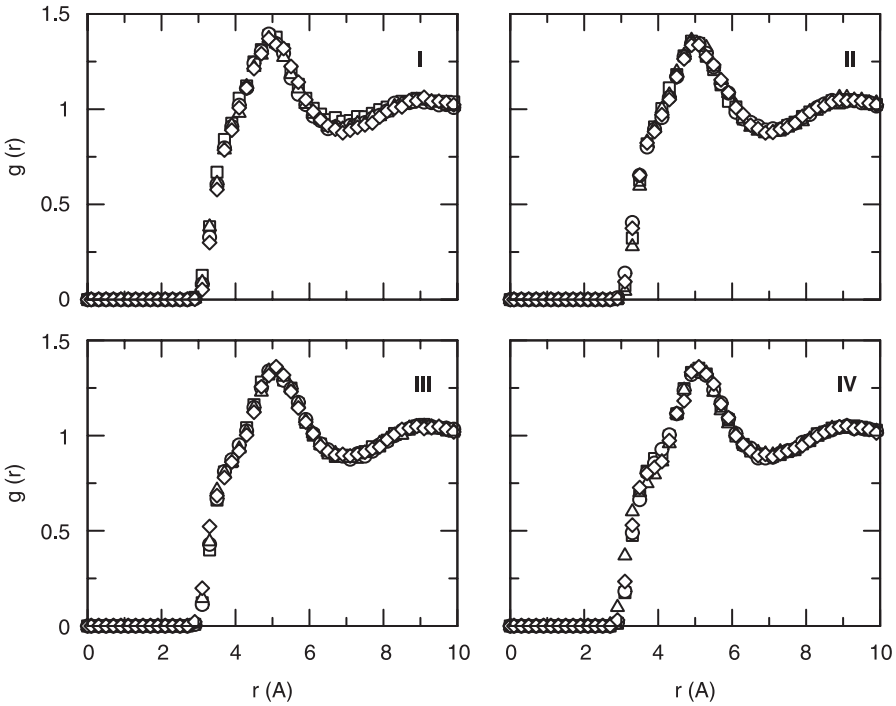

Figure 5. Radial distribution between CH_3 and oxygen for DME. Plot (I) contains model 1 (squares), model 2 (circle), model 3 (triangles) and model 4 (diamonds). Plot (II) contains model 5 (squares), model 6 (circle), model 7 (triangles) and model 8 (diamonds). Plot (III) contains model 9 (squares), model 10 (circle), model 11 (triangles) and model 12 (diamonds). Plot (IV) contains model 13 (squares), model 14 (circle), model 15 (triangles) and model 16 (diamonds).

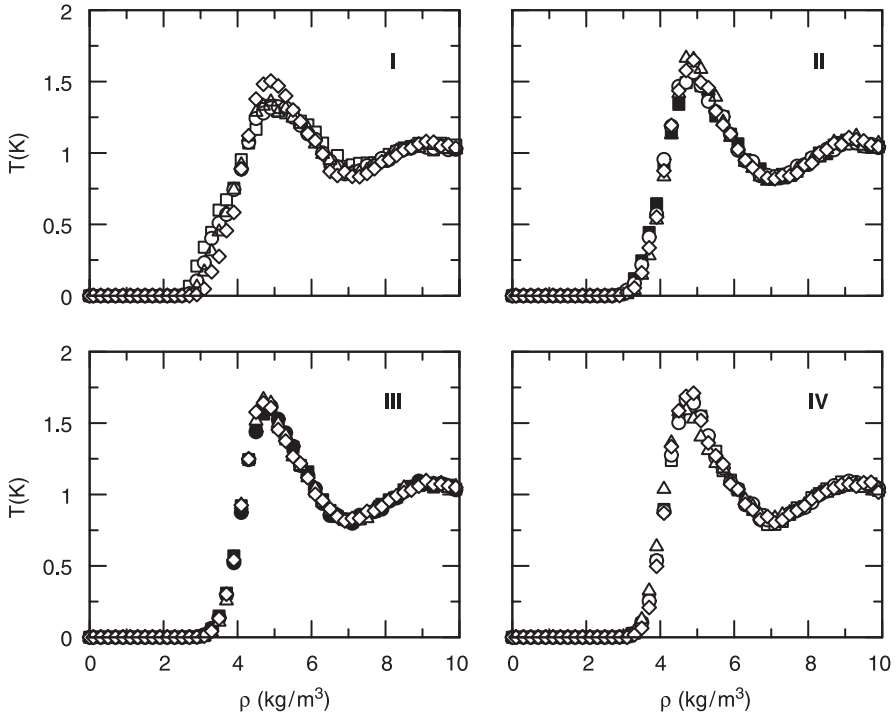

Figure 6. Radial distribution between oxygen and oxygen for DME. Plot (I) contains model 1 (squares), model 2 (circle), model 3 (triangles) and model 4 (diamonds). Plot (II) contains model 5 (squares), model 6 (circle), model 7 (triangles) and model 8 (diamonds). Plot (III) contains model 9 (squares), model 10 (circle), model 11 (triangles) and model 12 (diamonds). Plot (IV) contains model 13 (squares), model 14 (circle), model 15 (triangles) and model 16 (diamonds).

constraints on the parameter space has been shown to be effective in the parameter optimization process [10,11]. In addition to binary mixture phase behavior, it would be of interest to identify other pure component properties that would be effective in reducing the number of candidate parameter sets. Quantities of interest for further study include the surface tension as well as the viscosity.

Acknowledgements

The authors gratefully acknowledge financial support from the National Science Foundation (CTS-0522005) and Ganesh Kamath for helpful discussions.

References

[1] T.A. Halgen. Merck molecular force field. I. Basis, form, scope, parameterization, and performance of MMFF94. *J. Comp. Chem.*, **17**, 553 (1996).
[2] W.L. Jorgensen, D.S. Maxwell, J. Tirado-Rives. *J. Am. Chem. Soc.*, **118**, 11225 (1996).
[3] W.D. Cornell, P. Cieplak, C.I. Bayley, I.R. Gould, K.M. Merz Jr., D.M. Ferguson, D.C. Spellmeyer, T. Fox, J.W. Caldwell, P. Kollman. *J. Am. Chem. Soc.*, **117**, 5179 (1995).
[4] A.D. MacKerell, D. Bashford, M. Bellott, R.L. Dunbrack, J.D. Evanseck, M.J. Field, S. Fischer, J. Gao, H. Guo, S. Ha, D. Joseph-McCarthy, L. Kuchnir, K. Kuczera, F.T.K. Lau, C. Mattos, S. Michnick, T. Ngo, D.T. Nguyen, B. Prodhom, W.E. Reither, B. Roux, M. Schlenkrich, J.C. Smith, R. Stote, J. Straub, M. Watanabe, J. Wiorkiewicz-Kuczera, D. Yin, M. Karplus. *J. Phys. Chem. B*, **102**, 3586 (1998).
[5] X. Daura, A. Mark, W.F. Van Gunsteren. *J. Comp. Chem.*, **19**, 535 (1998).
[6] M.G. Martin, J.I. Siepmann. *J. Phys. Chem. B*, **102**, 2569 (1998).
[7] P. Ungerer, C. Beauvais, J. Delhommelle, A. Boutin, B. Rousseau, A.H. Fuchs. *J. Chem. Phys.*, **112**, 5499 (2000).
[8] S.K. Nath, F.A. Escobedo, J.J. de Pablo. *J. Chem. Phys.*, **108**, 9905 (1998).
[9] J.R. Errington, A.Z. Panagiotopoulos. *J. Phys. Chem. B*, **103**, 6314 (1999).
[10] J.J. Potoff, J.I. Siepmann. *AICHE J.*, **47**, 1676 (2001).
[11] G. Kamath, N. Lubna, J.J. Potoff. *J. Chem. Phys.*, **123**, 124505 (2005).
[12] G. Kamath, G. Georgiev, J.J. Potoff. *J. Phys. Chem. B*, **109**, 19463 (2005).
[13] A.M. Arkharov, S.D. Glukhov, L.V. Grekhov, A.A. Zherdev, N.A. Ivashchenko, D.N. Kalinin, A.V. Sharaburin, A.A. Aleksandov. *Petrol. Chem. Eng.*, **39**, 330 (2003).
[14] C.Y. Tsang, W.B. Streett. *J. Chem. Eng. Data*, **26**, 155 (1981).
[15] E. Chang, J.C.G. Calado, W.B. Streett. *J. Chem. Eng. Data*, **27**, 293 (1982).
[16] J.J. Potoff, J.R. Errington, A.Z. Panagiotopoulos. *Mol. Phys.*, **97**, 1073 (1999).
[17] H.A. Lorentz. *Ann. Phys.*, **12**, 127 (1881).
[18] D.C. Berthelot, R. Hebd. *Seanc. Acad. Sci. Paris*, **126**, 1703 (1898).
[19] J.M. Stubbs, J.J. Potoff, J.I. Siepmann. *J. Phys. Chem. B*, **108**, 17596 (2004).
[20] M.G. Martin, I. Siepmann. *J. Phys. Chem. B*, **103**, 4508 (1999).
[21] I.R. McDonald. *Mol. Phys.*, **23**, 41 (1972).
[22] W.W. Wood. *J. Chem. Phys.*, **48**, 415 (1968).
[23] P.P. Ewald. Calculation of optic and electrostic lattice potential. *Ann. Phys.*, **64**, 253 (1921).
[24] M.P. Allen, D.J. Tildesley. *Computer Simulation of Liquids*, 1st ed., Oxford University Press, Oxford (1987).
[25] J. Perez-Pellitero, P. Ungerer, G. Orkoulas, A.D. Mackie. Critical point estimation of the Lennard-Jones pure fluid and binary mixtures. *J. Chem. Phys.*, **125**, 54515 (2006).
[26] J. Stoll, J. Vrabec, H. Hasse. *AICHE J.*, **49**, 2187 (2003).
[27] J. Stoll, J. Vrabec, H. Hasse. *Fluid Phase Equilib.*, **209**, 29 (2003).
[28] K.S. Pitzer. *J. Am. Chem. Soc.*, **77**, 3427 (1955).
[29] K.S. Pitzer, D.Z. Lippmann, R.F. Curl, C.M. Huggins, D.E. Petersen. The volumetric and thermodynamic properties of fluids. II. Compressibility factor, vapor pressure and entropy of vaporization *J. Am. Chem. Soc.*, **77**, 3433 (1955).
[30] R.C. Reid, J.M. Prausnitz, T.R. Sherwood. *The Properties of Gases and Liquids*, McGraw-Hill, New York (1977).
[31] J.S. Rowildson, B. Widom. *Molecular Theory of Capillarity*, Clarendon Press, Oxford (1982).
[32] J.S. Rowlinson, F.L. Swinton. *Liquids and Liquid Mixtures*, 3rd ed., Butter worth, London (1982).
[33] V.G. Privman, G.L. Trigg (Eds.). *Encyclopedia of Applied Physics*, 23, p. 41, Wiley-VCH, Berlin (1998).
[34] R.M. Kennedy, M. Sagenkanhn, J.G. Aston. The heat capacity and entropy, heats of fusion and vaporization, and the vapor pressure of dimethyl ether. The density of gaseous dimethyl ether. *J. Am. Chem. Soc.*, **63**, 2267 (1941).
[35] Weast R.C. Ed. *Crc Handbook of Chemistry and Physics* (62nd ed., Crc Press, 1981–82).
[36] F.A. Momany. Determination of partial atomic charges from *ab initio* molecular electrostatic potentials. Application to formamide, methanol, and formic acid. *J. Phys. Chem.*, **82**, 592 (1978).
[37] S.R. Cox, D.E. Williams. *J. Comput. Chem.*, **2**, 304 (1981).
[38] C.M. Breneman, K.B. Wiberg. Determining atom-centered monopoles from molecular electrostatic potentials. The need for high sampling density in formamide conformational analysis. *J. Comput. Chem.*, **11**, 361 (1990).
[39] M.J. Frisch, G.W. Trucks, H.B. Schlegel, G.E. Scuseria, M.A. Robb, J.R. Cheeseman, J.A. Montgomery Jr., T. Vreven, K.N. Kudin, J.C. Burant, J.M. Millam, S.S. Iyengar, J. Tomasi, V. Barone, B. Mennucci, M. Cossi, G. Scalmani, N. Rega, G.A. Petersson, H. Nakatsuji, M. Hada, M. Ehara, K. Toyota, R. Fukuda, J. Hasegawa, M. Ishida, T. Nakajima, Y. Honda, O. Kitao, H. Nakai, M. Klene, X. Li, J.E. Knox, H.P. Hratchian, J.B. Cross, V. Bakken, C. Adamo, J. Jaramillo, R. Gomperts, R.E. Stratmann, O. Yazyev, A.J. Austin, R. Cammi, C. Pomelli, J.W. Ochterski, P.Y. Ayala, K. Morokuma, G.A. Voth, P. Salvador, J.J. Dannenberg, V.G. Zakrzewski, S. Dapprich, A.D. Daniels, M.C. Strain, O. Farkas, D.K. Malick, A.D. Rabuck, K. Raghavachari, J.B. Foresman, J.V. Ortiz, Q. Cui, A.G. Baboul, S. Clifford, J. Cioslowski, B.B. Stefanov, G. Liu, A. Liashenko, P. Piskorz, I. Komaromi, R.L. Martin, D.J. Fox, T. Keith, M.A. Al-Laham, C.Y. Peng, A. Nanayakkara, M. Challacombe, P.M.W. Gill, B. Johnson, W. Chen, M.W. Wong, C. Gonzalez, J.A. Pople. *Gaussian 03*, Revision C.02 Gaussian, Inc., Wallingford CT (2004).
[40] N. Lubna, G. Kamath, J.J. Potoff, N. Rai, I.J. Siepmann. Transferable potentials for phase equilibria. 8. United-atom description for thiols, sulfides, disulfides, and thiophene. *J. Phys. Chem. B*, **109**, 24100 (2005).
[41] V.M. Anisimov, G. Lamoureux, I.V. Vorobyov, N. Huang, B. Roux, A.D. MacKerell Jr.. *J. Chem. Theory Comput.*, **1**, 153 (2005).
[42] J. Delhommelle, C. Tschirwitz, P. Ungerer, G. Granucci, P. Millie, D. Pattou, A.H. Fuchs. Article title is: Application of the multimolecule and multiconformational RESP methodology to biopolymers: Charge derivation for DNA, RNA, and proteins. *J. Phys. Chem. B*, **104**, 4745 (2000).
[43] P. Cieplak, W.D. Cornell, C. Bayly, P. Kollman. Application of the multimolecule and multiconformational RESP methodology to biopolymers: charge derivation for DNA, RNA, and proteints. *J. Comp. Chem.*, **16**, 1357 (1995).
[44] N.B. Vargaftik. *Handbook of Physical Properties of Liquids and Gases: Pure Substances and Mixtures*, 2nd ed., Hemisphere, Bristol, PA (1983).